Article:
Namus, R., Rainforth, W.M., Huang, Y. et al. (2021) Effect of grain size and crystallographic structure on the corrosion and tribocorrosion behaviour of a CoCrMo biomedical grade alloy in simulated body fluid. Wear, 478-479. 203884. ISSN: 0043-1648

https://doi.org/10.1016/j.wear.2021.203884

Effect of grain size and crystallographic structure on the corrosion and tribocorrosion behaviour of a CoCrMo biomedical grade alloy in simulated body fluid

Righdan Namus[a, b], W. Mark Rainforth[a], Yi Huang[c,d], Terence G. Langdon[d]

[a] Department of Materials Science and Engineering, The University of Sheffield, Mappin Street, Sheffield, S1 3JD, UK.

[b] Mechanical Engineering Department, Faculty of Engineering, The University of Wasit, Kut, Iraq

[c] Department of Design and Engineering, Faculty of Science and Technology, Bournemouth University, Poole, Dorset BH12 5BB, UK

[d] Materials Research Group, Department of Mechanical Engineering, University of Southampton, Southampton SO17 1BJ, UK

Abstract

CoCrMo alloys are used in hip and knee replacements due to their excellent long-term survival rates. However, high failure rates have recently been observed associated with adverse tissue reactions. CoCrMo alloy surfaces undergo microstructural changes during wear, including the formation of ε-martensite and, occasionally, a nanocrystalline surface layer. It is not clear whether these changes are beneficial or detrimental to the performance of the component. Thus, high-pressure torsion (HPT) was employed to produce different grain sizes and crystallographic structures in a CoCrMo alloy and the corrosion and tribocorrosion behaviour were critically investigated as a function of grain size. The results reveal a degradation of the corrosion resistance for the HTP processed samples. The contributions of mechanical and corrosion material loss in tribocorrosion is also examined.

Keywords

CoCrMo biomedical grade alloy, high-pressure torsion, nanocrystalline structures, tribocorrosion.

1 Introduction

CoCrMo alloys have functioned as biomedical implants that have been extensively used in total hip replacements and hip resurfacing treatments for many years. These implants have demonstrated excellent performance with several having longevities of more than two decades [1]–[3]. For example, McKellop et al. [2] examined 21 metal-on-metal (MoM) hip

replacements using as-cast CoCrMo alloy and found that one-third of them lasted for more than 20 years.

The release of metal debris and ions has recently become a serious area of concern regarding the use of CoCrMo alloy MoM hip replacements [4]–[6]. Consequently. the Medicines and Healthcare Products Regulatory Agency (UK) and the Food and Drug Administration (US) issued alerts on the use of all MoM hip replacements, resulting in a sharp decline in the demand for these implants. The reason behind the abrupt change in the survivability of MoM implants is currently under debate with considerable focus on the femoral head design. However, it is clear that there is a direct relationship between the release of metal ions and implant failure, thereby indicating the significant role of corrosion in the performance of these implants.

CoCrMo alloy surfaces undergo significant microstructural changes during wear due to their low stacking-fault energy. These changes include the formation of mechanical twins, strain-induced martensite, and, under specific conditions, a nanocrystalline subsurface layer [7]–[13]. Mechanical twinning and the formation of strain-induced martensite are always observed and are even periodically present in the initial surfaces whereas the nanocrystalline layer has only been observed in some of these implants [9], [11]. Rainforth et al. [8] identified a 30–100 nm thick intermittent nanocrystalline surface layer when they analyzed site-specific cross-sections from high and low wear regions of an MoM CoCrMo implant. Fischer et al. [12] suggested the importance of the cyclic creep (ratcheting) in the shear zone in determining the wear debris formation. Namus et al. [14] demonstrated that a nanocrystalline layer formed during wear possessed superior mechanical properties to that of the starting surface. However, the nanocrystalline layer formation was associated with the highest wear rates observed, and its superior mechanical properties did not appear to be associated with a reduction in wear rate. However, a worn surface structure comprising a thin

intermittent nanocrystalline layer with extensive surface transformation to martensite microstructure exhibited an order of magnitude lower wear rate than the thick nanocrystalline layer. The difference in the wear rate was complicated by differences in the extent to which a tribolayer formed on the worn surface, with clear evidence that the formation of a tribolayer was associated with a reduction in wear rate. It was therefore not possible to differentiate the effect of the tribofilm from the changes in surface microstructure, such as the formation of a nanocrystalline layer. Moreover, it is not clear whether the formation of a nanocrystalline layer is simply a material response to the wear process or whether such dynamic changes actually influence the wear rate. Certainly, there have been no systematic studies that look at the effect of surface structure and grain size on the wear behaviour.

Another important factor is the effect of dynamic changes to the surface structure on corrosion resistance. Studies investigating the influence of crystal structure on the corrosion resistance of Co-based alloys have shown that a face-centred cubic (FCC) crystal structure exhibits better corrosion resistance than hexagonal close-packed (HCP) crystal structure [15], [16]. Thus, alloying element that stabilises the FCC structure would be expected to improve the corrosion resistance. Zhang et al. [17] studied the corrosion resistance of CoCrMo alloy in 2 wt% H_2SO_4 with different crystal structures and observed a different open circuit potential (OCP), but identical anodic behaviour, for both the FCC and HCP structures within the passive and transpassive regions. However, they demonstrated that the precipitation of σ or Mo-rich phases, or both, on the grain boundary of the HCP structure produces a heterogeneous microstructure that may function as preferential sites for oxide breakdown in the transpassive region. In addition, they noticed that, despite the important role of Cr in forming the oxide layer in the passive region, Mo effectively inhibits the dissolution in the transpassive region by attaching to the outermost layer of the oxide film. However, the

influence of grain size and crystallographic structure on the corrosion resistance of CoCrMo alloys in a protein containing solution has not been sufficiently documented.

There are several comprehensive studies [18], [19] on the means by which the synergism of mechanical loading and electrochemical reactions influence mechanical wear and corrosion rates. It has been confirmed that between 22 and 50% of the damage in different biological media is rationalised by this synergism which clearly demonstrates the importance of this effect.

It is clear that there has been no study looking at the effect of grain size on wear and corrosion, where the grain size is systematically changed in the starting surface. Accordingly, the objective of the present research is to investigate the corrosion and tribocorrosion behaviour of a CoCrMo alloy in a simulated biological fluid where the grain sizes and crystallographic structure had been changed by processing before the testing. The effects of grain size and phase constitution are also identified.

2 Experimental

2.1 Material and preparation

An as-cast low carbon CoCrMo alloy rod (10 mm diameter), with the chemical composition outlined in Table 1, was sliced into ~1.5 mm-thick disks in preparation for processing by high-pressure torsion (HPT). Both sides of the disks were ground in a standard manner with a 4000 emery paper finish to ensure perfectly parallel sides. The final thickness of the samples after grinding was ~0.8 mm.

Table 1

Chemical composition of the as-cast low carbon CoCrMo alloy rod

Element	Co	Cr	Mo	Mn	C	Fe	Si	Ni
wt%	64.91	27.48	5.25	0.45	> 0.05	0.32	0.42	0.16

The processing by HPT was performed at room temperature using the equipment described elsewhere [20]. Specifically, each disk was placed in a depression on the upper surface of a lower massive anvil and the anvil was then brought upwards so that the disk was also contained within a similar depression on the lower surface of a massive upper anvil. A pressure of 6.0 GPa was applied to the disk with the lower anvil rotated at a speed of 1 rpm so that the disk was subjected to torsional strain. Recent results have shown that the speed of the anvil rotation has minimal effect on the microstructures produced by HPT [21]. This type of processing is termed quasi-constrained HPT because, since the anvils are not touching during processing, a small portion of the material is squeezed outwards between the two anvils [22]. In the present experiments, processing of the alloy was performed through a total number of revolutions, N, of one and five turns. Thus, Cast-CoCrMo, HPT1, and HPT2 are used for the as-cast (unprocessed), 1-turn HPT processed, and 5-turns HPT processed samples, respectively.

After processing by HPT, the samples were ground and polished in a standard manner with 1 μm diamond and SilcoTM finishing to ensure an optimal surface finish. Stylus profilometry (Diktak, Veeco) was used to measure the surface roughness of the samples after polishing, which was less than 10 nm R_a for all starting surfaces.

The two HPT processed samples (HPT1 and HPT2) and the as-cast CoCrMo sample (Cast-CoCrMo), all with identical dimensions, were mounted in resin with a piece of graphite rod

(5 mm diameter) attached to the back of the samples to make them suitable for the corrosion and tribocorrosion cells.

2.2 Crystallographic structure

The crystal structures of all samples were analysed using Cu Kα radiation (λ = 1.54184 Å) X-ray diffraction (XRD, Bruker D2 Phaser) and 2θ = 30–60°. The relative amounts of FCC (f^{FCC}) and HCP (f^{HCP}) phases were estimated by measuring the integrated intensities of the $(200)_{FCC}$ and $(10\bar{1}1)_{HC}{}^{P}$ XRD peaks, I_{200}^{FCC} and $I_{10\bar{1}1}^{HCP}$, respectively. The weight fraction of the HCP phase was calculated using the Sage and Gillaud formula [23]:

$$f^{HCP}(wt\%) = \frac{I_{10\bar{1}1}^{HCP}}{I_{10\bar{1}1}^{HCP} + 1.5\, I_{200}^{FCC}} \qquad 1$$

The microstructure of the Cast-CoCrMo sample was analysed using the ion channeling contrast technique in focused ion beam (FIB, FEI Quanta 200 3D SEM/FIB, the Netherlands). The HPT1 and HPT2 samples were analysed using the electron channeling contrast imaging technique in a scanning electron microscope (SEM, InspectF 50, FEI, the Netherlands).

2.3 Nanomechanical properties

Nanoindentation (Micro Material Vantage, UK) was used to examine the mechanical properties of the starting surfaces. A spherical diamond indenter (20 μm radius) was used to construct the indentation stress-strain curve and measure the indentation compressive yield stress, σ_y. The partial unload function was used where this function consisted of 40 successive cycles each of which included loading in a second, holding for one second, and partial unloading to half of the load in a second. The indentation began with a 0.3 mN load which was incrementally increased to a maximum load of 500 mN. Twelve separate indentations were performed in a 2 × 3 grid with 10 μm distance between every two

indentations and the average of σ_y was calculated. A standard Berkovich indenter was also used to measure the indentation hardness (H) and the modulus of elasticity (E) of the three materials. For this measurement, a standard trapezoidal load function was used. The function consisted of loading in 5 s to a 30 mN load, holding for 5 s, and unloading in 5 s. A grid of 5 × 5 indentations was obtained to calculate the average of H and E. The distance between every two indents was 10 μm. All nanoindentation tests were repeated on three different samples to ensure a good reproducibility.

2.4 Corrosion characterisation

The samples were immersed in freshly prepared simulated body fluids. Newborn bovine calf serum (First Link (UK) Ltd.) was diluted and buffered to a 25% (v/v) solution in an aqueous solution of phosphate-buffered saline (Sigma-Aldrich). Ultrapure water (Alfa Aesar) was used in the preparation of the solution to yield a solution with a protein content of 15.8 g/L which is within the range of normal protein content in the human body fluid of healthy humans [24], [25]. The pH of the solution was 7.4 and the temperature of the tests was 37 °C. Corrosion and tribocorrosion studies were performed by using a corrosion and tribocorrosion cell. This was a traditional three-electrode cell with a saturated calomel electrode (SCE) as the reference electrode RE, a platinum wire as the counter electrode, and with the tested material as the working electrode. The cell also had a heater and temperature sensor to control the test temperature. The volume of the cell was ≈100 mL. The cell was connected to a Bruker UMT Multi-Specimen Test System to control the temperature and record the normal and lateral forces (Fx, Fz respectively) and the coefficient of friction COF in the tribocorrosion testing. The cell was also connected to a VersaSTAT 3F potentiostat/galvanostat (Princeton Applied Research, USA) to control the potential.

The potentiodynamic curve for all samples was obtained from -0.25 V vs OCP to 0.7 V vs RE at a scan rate of 0.5 mV/s. Corrosion parameters such as the corrosion current density (i_{corr}), corrosion potential (E_{corr}), and anodic and cathodic slopes (β_a and β_c, respectively) were calculated using CView software. All potentiodynamic curves were repeated on three different samples with good reproducibility.

2.5 Work procedure for tribocorrosion testing

Reciprocating sliding wear tests were conducted in a ball-on-plate configuration which conformed to ASTM G133. The counterpart was an alumina ball with 5 mm diameter and 99% purity (Oakwade Ltd., UK) with the ball used as an inert counterface. The load was 0.5 N which produced a mean initial contact pressure of ~450 MPa. A high initial contact pressure was deliberately selected to ensure a complete removal of the robust chromium oxide from the surface at the beginning of the rubbing. The wear track was located at a position on the sample at least 2 mm from the centre to avoid the lower hardness region in the centre of the HPT-processed samples [26], [27]. All tribocorrosion tests were conducted at a temperature of 37 °C in the same simulated body fluid as used in the corrosion testing. Tests were undertaken using reciprocating motion with a stroke length of 2 mm at 5 Hz which gives a linear sliding speed was 20 mm/s. For normal adults the gait speed is typically up to 1 m/s for walking which, when considering the dimensions of the femoral head and the extension during walking, equates to a speed of 20-28 mm/s (depending on a number of factors such as male vs female, size of the individual and now active). Therefore, the selected speed is at the lower end of the normal gait speed but within the normal range. The testing time was 3 h giving at total of 54000 cycles.

Testing was performed under OCP and at a –0.9 V cathodic potential. According to G119 ASTM standard, the total material loss T is defined as the wear rate under OCP conditions;

the material wear rate without corrosion interaction W_0 should be determined for a specimen polarised one volt cathodically with respect to E_{corr}. However, it is experimentally observed that 1 V cathodic polarisation vs E_{corr} in the studied system causes a degradation in the solution and heavy adsorption of protein on the surface of the CoCrMo alloy which may affect the results of the current study. Thus, –0.9 V cathodic potential was chosen to reduce this effect. The influence of cathodic potential on the adsorption of protein on the corrosion and tribocorrosion behavior of CoCrMo alloys in simulated body fluid has previously been studied [28], [29]. No hydrogen evolution was observed under the used cathodic potential. During the OCP tests the loading and rubbing were applied after waiting for 30 min for the OCP to become stabilised. During cathodic testing, the potential was applied for 30 min for the cathodic current to be stabilised followed by loading and rubbing. All tribocorrosion tests were repeated on two different specimens and several times on the same specimen and generally exhibited good reproducibility. The standard error of mean was used to calculate the error bars.

A 3D optical microscope (Bruker, Contour GT, USA) was used to determine the wear volume. Examination of the alumina ball after all tests showed intact counterfaces and therefore the wear of the contour body was not included in the wear rate analysis. A series of images were taken along the wear track and combined together to give precise and statistically meaningful wear volumes from the wear tracks. The specific wear rate, K, in $mm^3/N{\cdot}m$ was calculated using the standard relationship [30]:

$$K = \frac{V}{dL} \qquad 2$$

where V is the wear volume of material loss in mm^3, L is the normal load in N, and d is the total sliding distance in m.

The total material loss rate, T, stated in mm/year in tribocorrosion testing can be expressed as [31]:

$$T = W_C + C_W \quad (3)$$

$$W_C = W_0 + \Delta W_C \quad (4)$$

$$C_W = C_0 + \Delta C_W \quad (5)$$

where W_C and C_W represent the material loss due to mechanical wear and corrosion, respectively, in tribocorrosion, W_0 is the mechanical wear calculated from the wear test under cathodic potential and C_0 is the rate of corrosion material loss in the absence of wear. In practice, C_0 is essentially negligible for passive metals and alloys because it is extremely small ($C_W = \Delta C_W$). The wear rate (T, W_0) in mm/year can be calculated using the following equation [32]:

$$\text{Wear rate (mm/yr)} = \frac{8760\ V}{t\ SA} \quad (6)$$

where SA is the surface area of the wear track and t is the test time. In this equation, the constant 8760 is the number of hours in a year. ΔW_C is the change in wear rate due to corrosion (in mm/yr) and ΔC_W is the change in corrosion rate due to wear (in mm/year). ΔC_W is represented by:

$$\Delta C_W = k \frac{i_{wt}}{\rho} M \quad (7)$$

where i_{wt} is the flowing current from the wear track during rubbing, k is a constant (3.27×10^{-3} mm·g/μA·cm·year), M is the equivalent weight (24.17 g/mol) and ρ is the density (8.5 g/cm^3).

The mean driving force for this material loss under the OCP testing conditions is the galvanic couple that forms between the depassivated surface (wear track) and the passivated surface (the remaining surface). The galvanic coupling model suggested by Vieira et al. [33], and

applied to different materials by Papageorgiou and Mischler [34], was used to calculate the current flow from the wear track ($i_{\omega t}$) as the following:

$$\log i_{\omega t} = \frac{\left(E_{corr} - E_{\omega t} + a_c - b_c \log\left(\frac{A_{wt}}{A_p}\right)\right)}{b_c} \qquad 8$$

where, $E_{\omega t}$ is the sliding potential, a_c and b_c are the Tafel constants calculated from the cathodic branch of the potentiodynamic curve [35], and A_{wt} and A_p are the surface areas of the wear track and the passive surface, respectively.

3 Results

3.1 Characterisation of the surfaces

Fig. 1 shows the XRD patterns for the Cast-CoCrMo, HPT1, and HPT2 samples. The dominant phase in the as-cast sample (Cast-CoCrMo) is FCC, with ~28 wt% HCP present. The weight fraction of the HCP phase increased to 51 wt% in the samples processed by HPT for 1 turn which is indicated by the increasing intensity of the $(10\bar{1}1)_{HCP}$ peak and the decreasing of $(200)_{FCC}$ peak. The microstructure of the HPT2 sample is dominated by the HCP phase (77%).

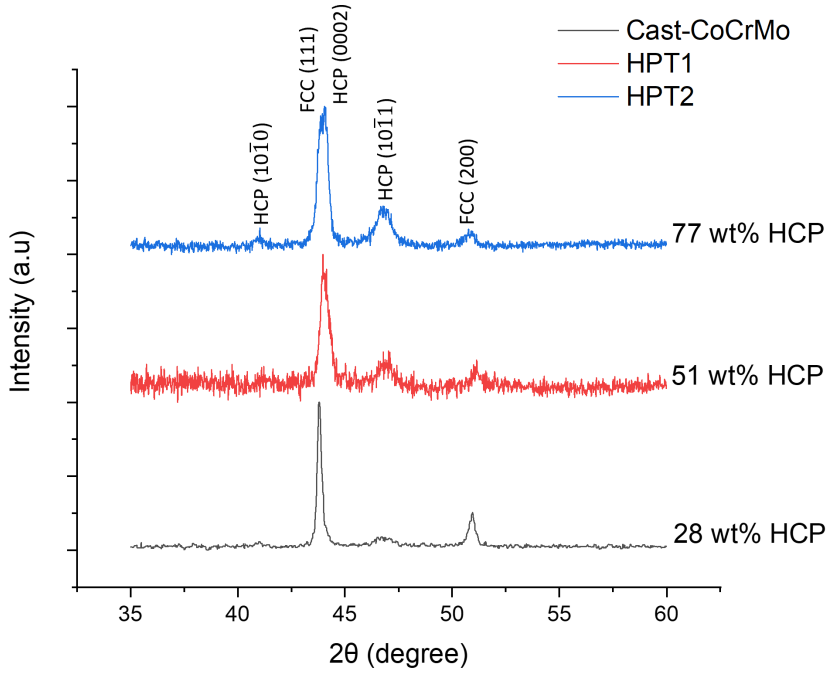

Fig. 1. XRD patterns for the Cast-CoCrMo, HPT1, and HPT2 samples. The wt% HCP significantly increases with the number of turns of HPT processing.

Fig. 2 gives ion channelling contrast images for Cast-CoCrMo and the electron channeling contrast images for the HPT1 and HPT2 surfaces. The average grain size measured by the linear intercept method is 7.4 μm for the Cast-CoCrMo sample. The microstructure of the HPT1 sample exhibits a mixture of ultrafine grains and nanocrystalline structures but the imaging of the HPT2 sample reveals a fully nanocrystalline structure.

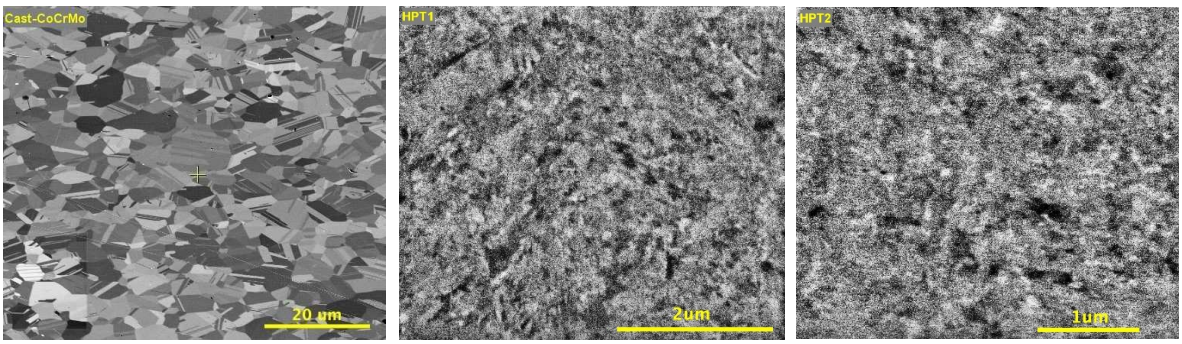

Fig. 2. Ion channelling contrast image for the Cast-CoCrMo sample and electron channelling contrast imaging for the HPT1 and HPT2 samples.

3.2 Mechanical properties

The mechanical properties of the as-cast (Cast-CoCrMo) and HPT processed (HPT1 and HPT2) CoCrMo alloy samples were examined using nanoindentation. Fig. 3 shows a typical example of the indentation stress-strain curves for the Cast-CoCrMo, HPT1, and HPT2 samples. The curves were used to calculate the uniaxial indentation compressive yield stress, σ_y. In the indentation stress-strain curve, three deformation regimes are identified based on the relationship between the mean contact pressure (p_m) and the indentation compressive yield stress (σ_y). When $p_m < 1.1\sigma_y$, the material is elastically deformed. When $p_m = 1.1\sigma_y$, first yielding occurs at 0.5a below the surface (Hertzian contact theory). When $1.1\sigma_y < p_m < C\sigma_y$, the material deforms plastically but is surrounded by elastically deformed material [36]. Thus, this point is called the initial yielding (σ_I) [36], [37]. The constant (C) is a material and indenter geometry dependent factor.

Fig. 4 shows the mechanical properties for Cast-CoCrMo, HPT1, and HPT2. There is a noticeable enhancement in the mechanical properties of the HPT-processed samples. H and σ_y increase continuously with the numbers of turns in the HPT processing and this is associated with the formation of ultrafine grains and nanocrystalline structures for HPT1 and HPT2, respectively. The value of E slightly decreased for the HPT-processed samples, probably due to the change in the crystallographic structures of these samples.

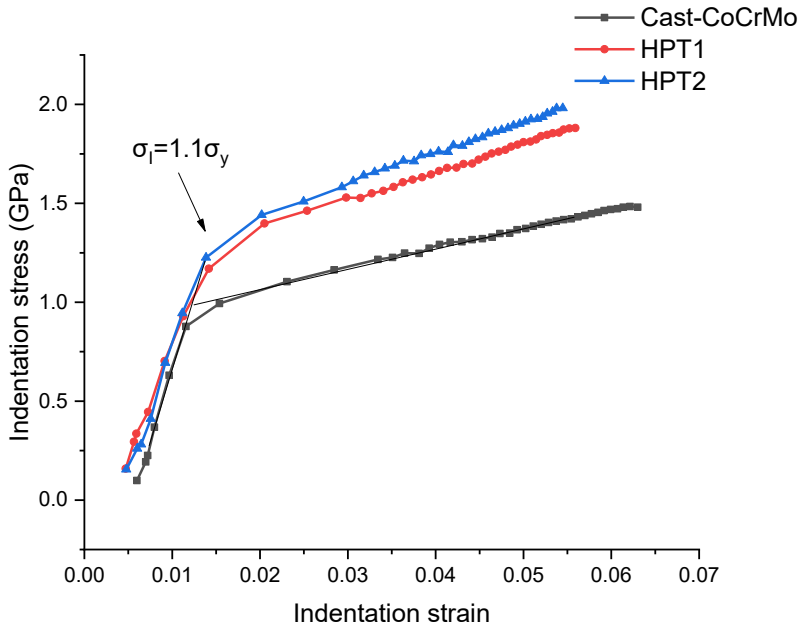

Fig. 3. A typical example of the indentation stress-strain curves for the Cast-CoCrMo, HPT1, and HPT2 samples.

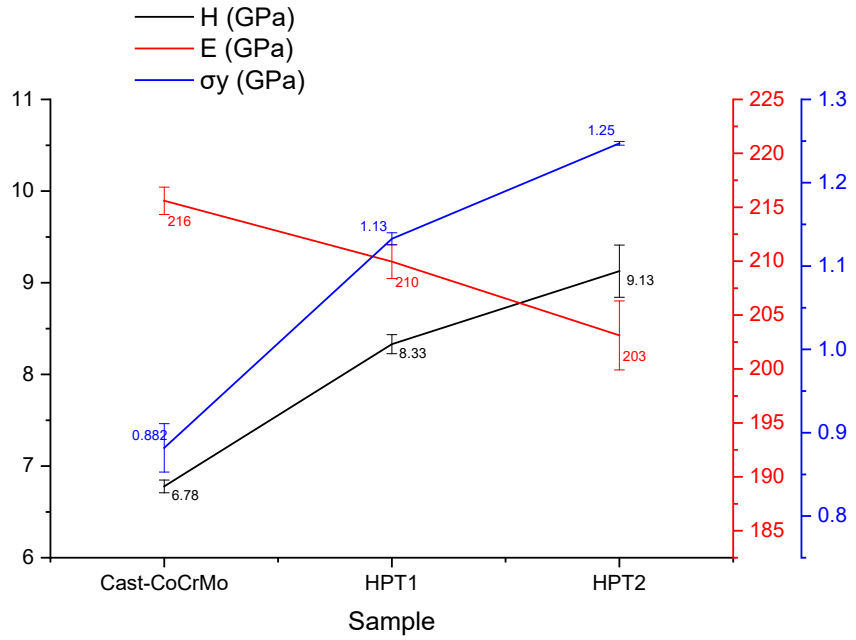

Fig. 4. The mechanical properties of all samples.

3.3 Corrosion investigation

The potentiodynamic polarisation curves and the results of the Tafel extrapolation method for the Cast-CoCrMo, HPT1, and HPT2 samples are shown in Fig. 5 and Table 2. The corrosion current density (i_{corr}) linearly increased for Cast-CoCrMo, HPT1 and HPT2. However, the passive current density I_p remained unchanged for Cast-CoCrMo and HPT1 but exhibited a 9-times increase for the HPT2 sample. There was no significant change in E_{corr} for the three samples tested in the simulated body fluid at 37 °C.

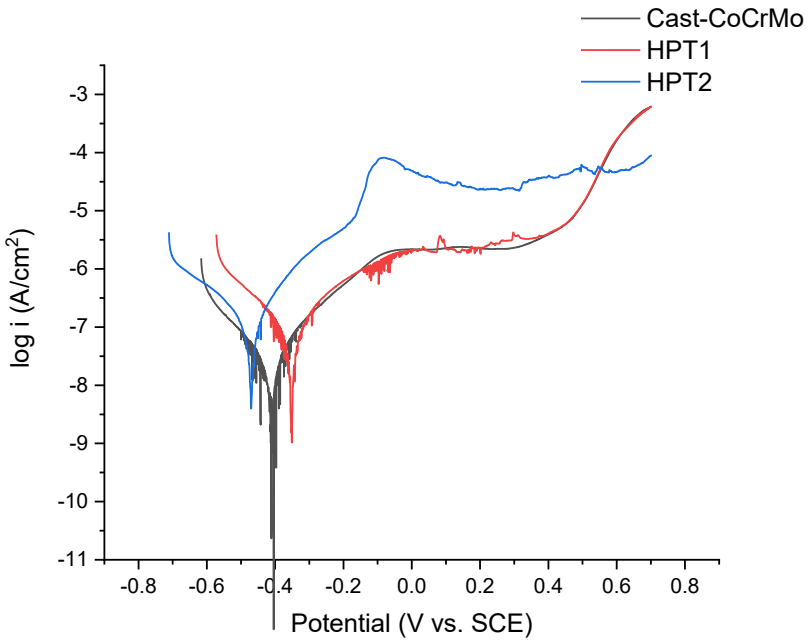

Fig. 5. Potentiodynamic curves for the Cast-CoCrMo, HPT1 and HPT2 CoCrMo alloy samples in the biological fluid at 37 °C.

Table 2

Corrosion parameters calculated using the Tafel extrapolation method for the Cast-CoCrMo, HPT1, and HPT2 CoCrMo alloys tested in the simulated body fluid at 37 °C

Sample	E_{corr} (V vs. SCE)	i_{corr} (nA/cm^2)	β_c (mV)	β_a (mV)	I_p ($\mu A/cm^2$)	CR (mm/yr) $\times 10^{-4}$
Cast-CoCrMo	-0.41	24.5±2.8	164	136	2.14±0.02	2.34
HPT1	-0.35	89.4±11	187	161	2.1±0.03	8.53
HPT2	-0.46	164±15.5	258	154	18±0.86	15.6

3.4 Tribocorrosion behaviour

All of the results of the tribocorrosion tests under OCP and cathodic potential are summarized in Tables 3 and 4, respectively. Fig. 6 gives the sliding potential as a function of time for the Cast-CoCrMo, HPT1 and HPT2 samples in the simulated body fluid at 37 °C under OCP conditions. For all samples, the potential shifted cathodically by ~125–150 mV when rubbing started.

Fig. 7 shows the specific wear rate (K) for the Cast-CoCrMo, HPT1 and HPT2 samples tested under OCP and cathodic potential. All samples exhibited values of K one order of magnitude less under the cathodic potential compared to under OCP testing conditions. Interestingly, HPT1 and HPT2 samples exhibited the same K as the Cast-CoCrMo sample at the cathodic potential despite having superior mechanical properties. Under OCP testing conditions, K was ~20% greater for HPT1 and ~11% less for HPT2 compared to the as-cast alloy (Cast-CoCrMo sample).

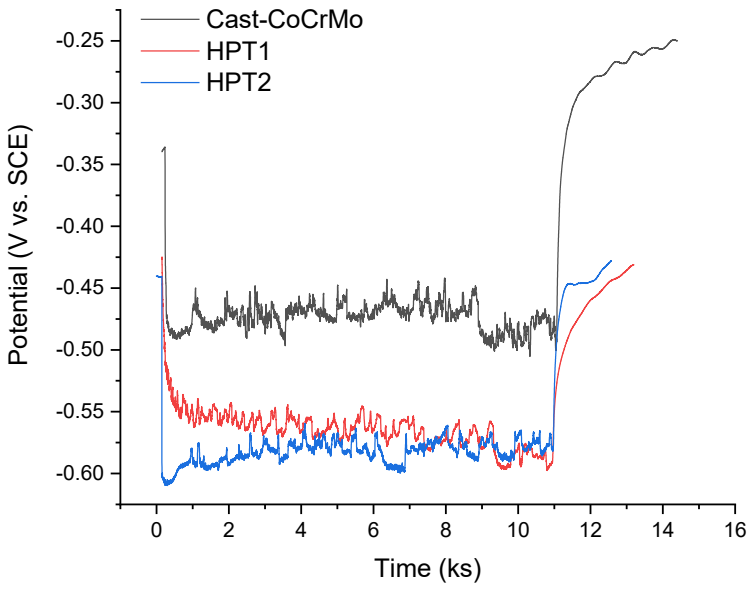

Fig. 6. Sliding potential as function of time for the Cast-CoCrMo, HPT1, and HPT2 CoCrMo alloy samples in the simulated body fluid at 37 °C.

Table 3

Results of tribocorrosion testing for the Cast-CoCrMo, HPT1, and HPT2 CoCrMo alloy samples in the simulated body fluid at 37 °C and under the OCP

Sample	**COF**	**V** mm^3 $\times10^{-4}$	**SA** mm^2	**K** $mm^3/N\ m$ $\times10^{-6}$	**T** mm/yr	**$E_{sliding}$** (mV)	**log (A_w/A_0)**
Cast-CoCrMo	0.19	3.99	0.384	3.69±0.23	3±0.14	–480	–2.6
HPT1	0.2	4.64	0.412	4.51±0.22	3.28±0.09	–588	–2
HPT2	0.18	3.54	0.462	3.28±0.16	2.23±0.096	–585	–2.22

b_c	**a_c**	**OCP**	**E_{corr}**	**i_{wt}**	**C_w**	**ΔW_c**

		(mV)	(mV)	μA/cm^2	mm/yr	mm/yr
0.33	–1.65	–350±12	–410	8.4	0.08	2.26
0.36	–1.5	–312±16	–350	35.92	0.34	2.19
0.46	–1.77	–450±14	–460	44.33	0.42	1.14

Table 4

Tribocorrosion testing results for Cast-CoCrMo, HPT1 and HPT2 CoCrMo alloy samples in the simulated body fluid at 37°C and –0.9 V cathodic potential

Samples	**COF**	**V** $mm^3 \times 10^{-5}$	**SA** mm^2	**K** $mm^3/N\ m \times 10^{-7}$	**W_0** mm/y
Cast-CoCrMo	0.21	4.9	0.21	4.54±0.46	0.68±0.054
HPT1	0.2	5.4	0.21	5±0.24	0.75±0.042
HPT2	0.19	4.6	0.12	4.26±0.29	0.67±0.045

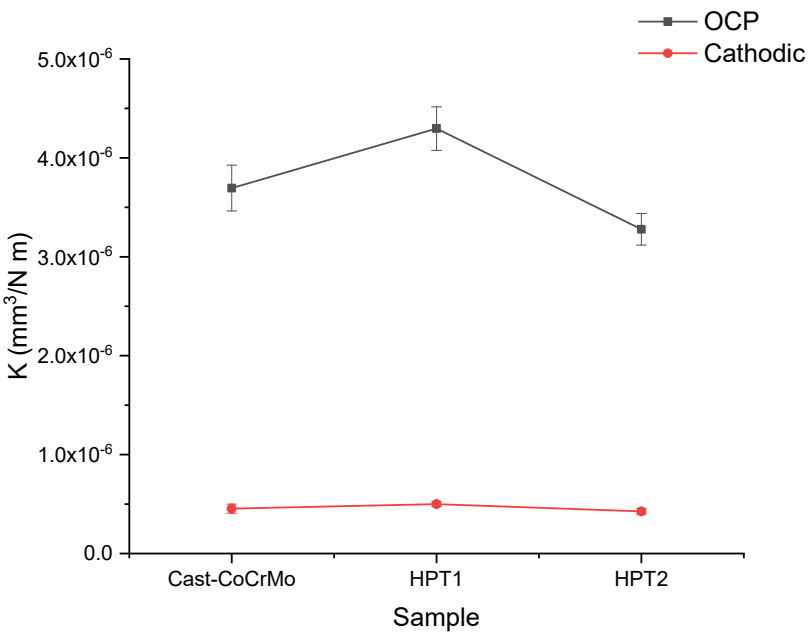

Fig. 7. Specific wear rate (K) for the Cast-CoCrMo, HPT1, and HPT2 samples at OCP and cathodic potential

Further investigation into the contributions to tribocorrosion are shown in Fig. 8. The corrosion contribution C_W or ΔC_W, since they are proposed to be equal for passive metals and alloys, increase almost linearly for Cast-CoCrMo, HPT1 and HPT2. However, the contribution of the pure mechanical wear, W_0, was almost constant, showing no correlation with crystallographic structure or grain-size. The values of ΔW_C demonstrated a slight decrease between the Cast-CoCrMo and HPT1 samples followed by ~50% decrease for the HPT2 sample.

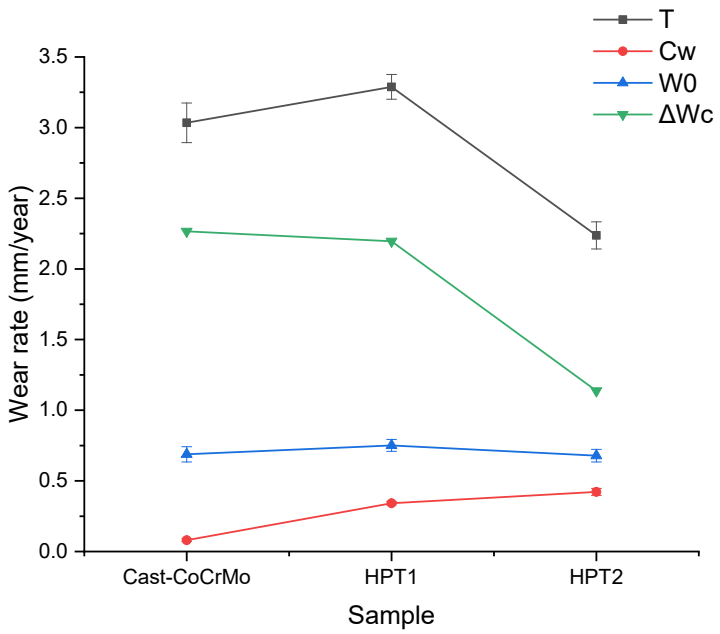

Fig. 8. Contributions to material loss in the tribocorrosion tests for the Cast-CoCrMo, HPT1, and HPT2 samples.

3.5 Wear scar morphology

The wear scar morphology for all tests are shown in Fig. 9. At the OCP, the worn surfaces of the Cast-CoCrMo samples are etched in such a way that the microstructure is revealed. This is possibly due to the corrosive-abrasive wear mechanism under these conditions. Abrasive ploughing grooves are also observed on this wear scar. At the cathodic potential, the ploughing abrasion mechanism for Cast-CoCrMo appears to be dominant, with no evidence of micro-cutting which potentially indicates an absence of wear debris trapping in the wear scar. The wear scars of the HPT1 and HPT2 specimens at the cathodic potential appear similar to those of the Cast-CoCrMo sample under the same potential with a few relatively deep grooves at HPT2. Under the OCP, the HPT1 and HPT2 specimens exhibited the same corrosive-abrasive wear mechanism as the Cast-CoCrMo sample. The HPT1 and HPT2 samples displayed an increase in the extruded deformation lines on the wear scar and these are associated with an increase in the amount of ε-HCP (Fig. 1).

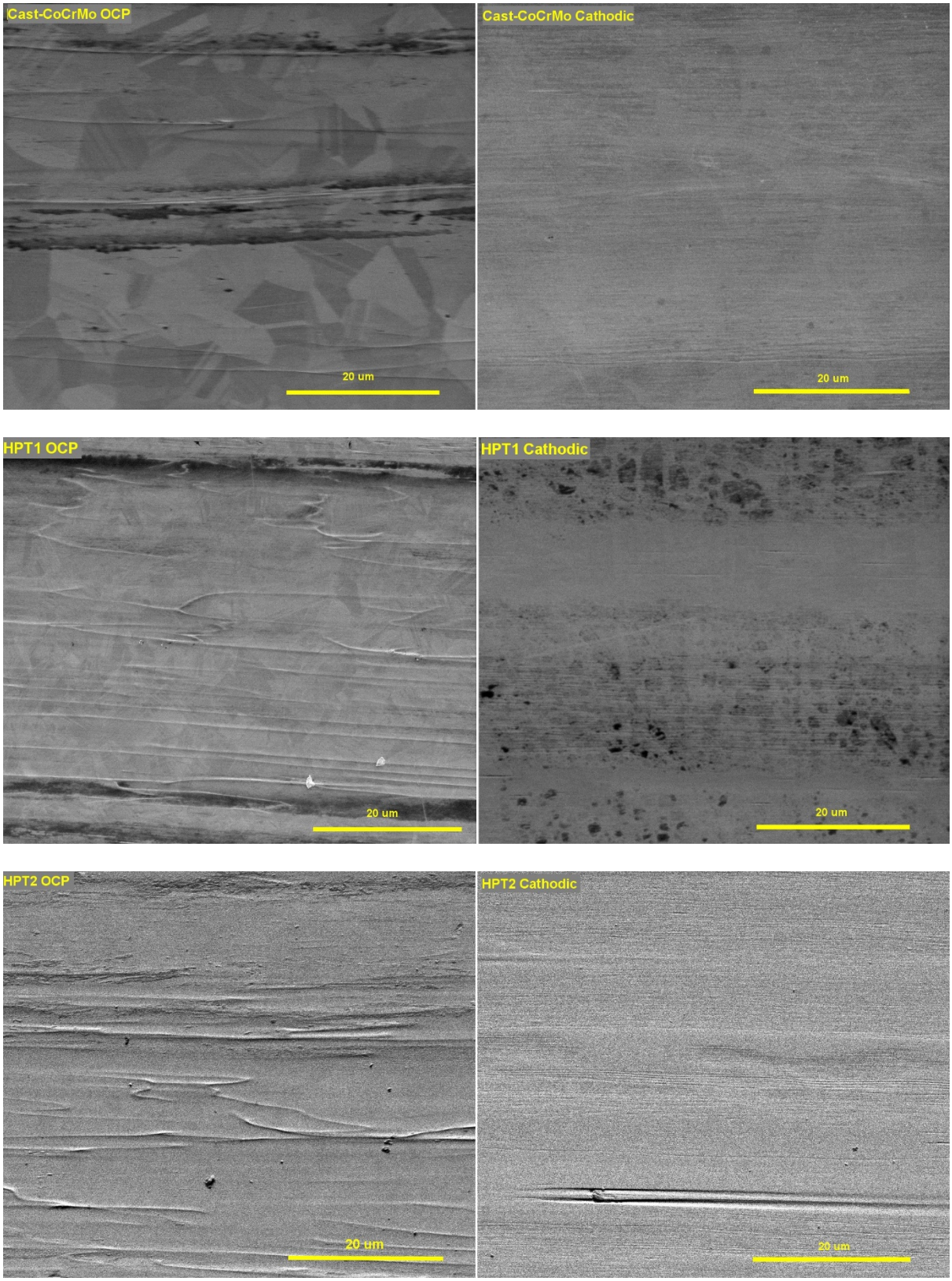

Fig. 9. SEM images of the worn surfaces of the Cast-CoCrMo, HPT1, and HPT2 samples at OCP and cathodic potential.

4 Discussion

Different grain sizes and crystallographic structures of the CoCrMo biomedical grade alloy were successfully produced by processing using HPT. The microstructure was a mixture of ultrafine grains and nanocrystalline structures for the HPT1 sample compared with a fully-nanocrystalline structure for the HPT2 sample (Fig. 2). As the numbers of turns in HPT processing increased, the crystallographic structure transformed from FCC-dominated to HCP-dominated structures (Fig. 1).

The potentiodynamic investigation revealed a degradation in the corrosion resistance of the CoCrMo alloys for the HPT1 and HPT2 samples compared to the Cast-CoCrMo sample. Based on earlier reports, the larger grain boundary density that exists in ultrafine grains and nanocrystalline structures facilitates more oxide nucleation sites and consequently faster growth rates for metallic materials [38]–[41]. The finer grain size increases the corrosion rate by enhancing the surface activity for active metals, whereas it improves the formation of the surface oxide layer for passive metals and alloys [38]. However, this does not necessarily correspond to an improved corrosion resistance for ultrafine-grained and nanograined passive metallic materials. For example, it was reported that an important reason for enhancing the passivation ability of nanograined 316L austenitic stainless steel is the increase in the diffusion rate of charged species across the passive film [39] and this indicates a less protective ability of the oxide layer. A linear increase in i_{corr} for Cast-CoCrMo, HPT1 and HPT2 is possibly because of forming a less resistive oxide layer on the finer-grained CoCrMo alloy, but this needs further investigation.

There is a discrepancy in the literature regarding the correlation between grain size and wear resistance. Purcek et al. [42] demonstrated that the use of equal-channel angular pressing for pure titanium led to a substantial increase in the mechanical properties while retaining an

adequate ductility, but with zero effect on the wear resistance. Furthermore, a negative effect of ultrafine grains on the wear resistance was also reported [43], [44] where this was attributed to the tribochemical reaction and the synergistic effect between oxidative and abrasive wear which effectively masks any improvement in the mechanical properties. By contrast, other researchers have reported that severe plastic deformation produces considerably finer grain sizes and thereby gives an enhanced wear resistance for commercially pure titanium [43], and an Al-Cu alloy [44].

A fundamental assumption was made that the application of the cathodic potential reduces the contribution of corrosion and the synergism between corrosion and mechanical wear in tribocorrosion to a minimum. Based on this assumption, the results in the present investigation (K at cathodic potential (Fig. 7) and W_0 (Fig. 8)) suggest that neither the grain size nor the crystallographic structure has an impact on the mechanical wear resistance of CoCrMo alloys in a simulated body fluid sliding against an alumina ball. However, in practice the effect of applying the cathodic potential on the solution chemistry and consequently to the tribological system behaviour should be taken into consideration.

Some researchers [28], [45] have reported that the application of a cathodic potential in a protein containing solution leads to the adsorption of a thicker proteinaceous layer on the surface of the CoCrMo alloy compared to that tested under the OCP and passive potential. This observation was attributed to the electrochemical reduction of the bovine serum albumin which was reported to influence the tribocorrosion behaviour of the CoCrMo alloy [29]. The adsorbed proteinaceous layer may provide, under these testing conditions, the same tribological conditions regardless of the material microstructure. The formation of a proteinaceous layer on the worn surfaces of the CoCrMo biomedical grade alloy under the same working conditions (cathodic potential and other testing conditions) used herein was

also observed [46]. This layer may form and squeeze out under the effect of cyclic contact events.

Under the present OCP testing conditions, where corrosion and mechanical wear occur concurrently, the change in corrosion due to wear, ΔC_W, increased in the order Cast-CoCrMo, HPT1, and HPT2. This increase is expected in view of the larger numbers of nucleation sites and the faster growth rate of the oxide layer for the finer grain size structures. By contrast, the noticeable reduction in the change in wear due to corrosion, ΔW_C, between Cast-CoCrMo and HPT2 enhanced the total tribocorrosion behaviour of the alloy. The slight decrease in ΔW_C between Cast-CoCrMo and HPT1, despite the considerable decrease in the grain size (Fig. 2), strongly suggests that the grain size has only a small effect on this tribocorrosion contribution under these testing conditions. Instead, the influence of increasing concentration of the HCP phase was more significant, particularly between HPT1 and HPT2. The results also suggest that a certain amount of the HCP phase is required in order to cause a significant decrease in ΔW_C. In this case, 51 wt% HCP phase gave no significant decrease, whereas a decrease was observed for 77 wt% HCP phase. This finding agrees with other results [47], [48] where the wear rate of self-mated CoCrMo alloys decreased as the HCP phase increased in such a way that the lowest and highest wear rates were achieved in HCP-HCP and FCC-FCC mating, respectively.

Mechanical grain refinement for CoCrMo biomedical grade alloy is always associated with increasing the wt.% of HCP causing a significant impact on the corrosion and tribocorrosion behaviour of this alloy as shown in Fig. 10.

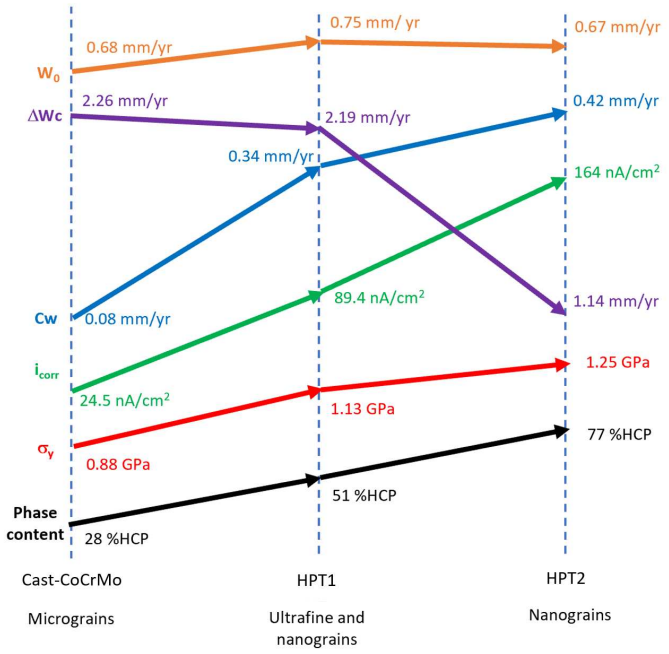

Fig. 10. A schematic diagram shows the effect of number of turns of HPT processing on the grain size and HCP wt.% and consequently of corrosion and tribocorrosion behaviour of CoCrMo biomedical grade alloy.

The practical failure of CoCrMo alloys as orthopaedics implants has been associated with the release of metallic ions [4]–[6] but the results of the present study clearly show that the corrosion contribution ΔC_W increased linearly for Cast-CoCrMo, HPT1, and HPT2. Further, the corrosion rate at static conditions for the nanocrystalline CoCrMo alloy is much higher than that for as cast alloy (Fig. 5 and Table 2). Thus, it is concluded that the formation of ultrafine grains and nanocrystalline structures is not beneficial for these implants despite the overall general improvement in the tribocorrosion behaviour of the alloy.

5 Conclusions

1. The microstructure of the as-cast CoCrMo alloy processed by HPT was a mixture of ultrafine grains and nanocrystalline structures after 1 turn of processing. However, the structure of the material became fully nanocrystalline after 5 turns of processing. The

weight fraction of the HCP phase increased with the numbers of turns in HPT processing.

2. The corrosion resistance C_0 for the CoCrMo alloy deteriorated for the samples processed by HPT.
3. The change in corrosion rate due to wear ΔC_W increased as the numbers of turns in HPT processing increased due to an elevation in the surface activity of the finer grain sizes. However, the change in wear rate due to corrosion ΔW_C decreased slightly between the Cast-CoCrMo and HPT1 samples but significantly decreased between the HPT1 and HPT2 samples which was attributed to the increase in the HCP phase weight fraction. As a result, the HPT2 sample exhibited the lowest total material loss.
4. Despite the overall improved tribocorrosion resistance, the results of this research reveal a detrimental influence in forming ultrafine-grains and nanograins on the surface of the CoCrMo alloy in orthopaedics implant applications because they serve to increase the change in corrosion due to wear and the corrosion rate at static conditions.
5. The mechanical wear W_0 did not change with grain size or phase content. This is because of the change in the electrolyte due to cathodic polarisation. Cathodic polarisation increases the adsorption of protein on the surfaces and thereby provides the same tribological conditions for the surfaces regardless of the microstructure and phase constitution of the alloy.

Acknowledgement

We wish to acknowledge the Henry Royce Institute for Advanced Materials (EPSRC Grant Number EP/R00661X/1) for the financial support and equipment access at Royce@Sheffield. Two of the authors were supported by the European Research Council under ERC Grant Agreement No. 267464-SPDMETALS (YH and TGL).

References

[1] D. W. Howie, R. W. McCalden, N. S. Nawana, K. Costi, M. J. Pearcy, and C. Subramanian, "The long-term wear of retrieved McKee-Farrar metal-on-metal total hip prostheses," *J. Arthroplasty*, vol. 20, no. 3, pp. 350–357, Apr. 2005, doi: 10.1016/j.arth.2004.09.028.

[2] H. McKellop S.H. Park, R. Chiesa, P. Doorn, B. Lu, P. Normand, P. Grigoris, H. Amstutz., "In vivo wear of 3 types of metal on metal hip prostheses during 2 decades of use," *Clin. Orthop. Relat. Res.*, no. 329 SUPPL., 1996, doi: 10.1097/00003086-199608001-00013.

[3] J. Daniel, C. Pradhan, H. Ziaee, P. B. Pynsent, and D. J. W. McMinn, "Results of Birmingham hip resurfacing at 12 to 15 years," *Bone Joint J.*, vol. 96-B, no. 10, pp. 1298–1306, Oct. 2014, Accessed: Aug. 11, 2018. [Online]. Available: http://online.boneandjoint.org.uk/doi/10.1302/0301-620X.96B10.33695.

[4] R. N. De Steiger, J. R. Hang, L. N. Miller, S. E. Graves, and D. C. Davidson, "Five-year results of the ASR XL acetabular system and the ASR hip resurfacing system: An analysis from the Australian Orthopaedic Association National Joint Replacement Registry," *J. Bone Jt. Surg. - Ser. A*, vol. 93, no. 24, pp. 2287–2293, Dec. 2011, doi: 10.2106/JBJS.J.01727.

[5] A. J. Smith, P. Dieppe, P. W. Howard, and A. W. Blom, "Failure rates of metal-on-metal hip resurfacings: Analysis of data from the National Joint Registry for England and Wales," *Lancet*, vol. 380, no. 9855, pp. 1759–1766, Nov. 2012, doi: 10.1016/S0140-6736(12)60989-1.

[6] F. W. Chan, J. D. Bobyn, J. B. Medley, J. J. Krygier, S. Yue, and M. Tanzer, "Engineering issues and wear performance of metal on metal hip implants," in *Clinical*

Orthopaedics and Related Research, 1996, no. 333, pp. 96–107, doi: 10.1097/00003086-199612000-00009.

[7] M. A. Wimmer, J. Loos, R. Nassutt, M. Heitkemper, and A. Fischer, "The acting wear mechanisms on metal-on-metal hip joint bearings: In vitro results," *Wear*, vol. 250–251, no. 1–12, pp. 129–139, Oct. 2001, doi: 10.1016/S0043-1648(01)00654-8.

[8] W. M. Rainforth, P. Zeng, L. Ma, A. N. Valdez, and T. Stewart, "Dynamic surface microstructural changes during tribological contact that determine the wear behaviour of hip prostheses: metals and ceramics," *Faraday Discuss.*, vol. 156, no. 0, pp. 41–57, Jul. 2012, doi: 10.1039/C2FD00002D.

[9] R. Pourzal, R. Theissmann, M. Morlock, and A. Fischer, "Micro-structural alterations within different areas of articulating surfaces of a metal-on-metal hip resurfacing system," *Wear*, vol. 267, no. 5–8, pp. 689–694, Jun. 2009, doi: 10.1016/j.wear.2009.01.012.

[10] P. Zeng, A. Rana, R. Thompson, and W. M. Rainforth, "Subsurface characterisation of wear on mechanically polished and electro-polished biomedical grade CoCrMo," *Wear*, vol. 332–333, pp. 650–661, May 2015, doi: 10.1016/j.wear.2015.02.007.

[11] R. Büscher and A. Fischer, "The pathways of dynamic recrystallization in all-metal hip joints," *Wear*, vol. 259, no. 7–12, pp. 887–897, Jul. 2005, doi: 10.1016/j.wear.2005.02.036.

[12] A. Fischer, S. Weiß, and M. A. Wimmer, "The tribological difference between biomedical steels and CoCrMo-alloys," *J. Mech. Behav. Biomed. Mater.*, vol. 9, pp. 50–62, May 2012, doi: 10.1016/j.jmbbm.2012.01.007.

[13] M. A. Wimmer, C. Sprecher, R. Hauert, G. Täger, and A. Fischer, "Tribochemical

reaction on metal-on-metal hip joint bearings A comparison between in-vitro and in-vivo results," *Wear*, vol. 255, no. 7–12, pp. 1007–1014, 2003, doi: 10.1016/S0043-1648(03)00127-3.

[14] R. Namus, P. Zeng, and W. M. Rainforth, "Correlation of the wear transition in CoCrMo alloys with the formation of a nanocrystalline surface layer and a proteinaceous surface film," *Wear*, vol. 376–377, pp. 223–231, 2017, doi: 10.1016/j.wear.2016.11.046.

[15] A. Human, B. Roebuck, and H. Exner, "Electrochemical polarisation and corrosion behaviour of cobalt and Co(W,C) alloys in 1 N sulphuric acid," *Mater. Sci. Eng. A*, vol. 241, no. 1–2, pp. 202–210, Jan. 1998, doi: 10.1016/S0921-5093(97)00492-9.

[16] M. Srivastava, V. Ezhil Selvi, V. K. William Grips, and K. S. Rajam, "Corrosion resistance and microstructure of electrodeposited nickel–cobalt alloy coatings," *Surf. Coatings Technol.*, vol. 201, no. 6, pp. 3051–3060, Dec. 2006, doi: 10.1016/J.SURFCOAT.2006.06.017.

[17] X. Zhang, Y. Li, N. Tang, E. Onodera, and A. Chiba, "Corrosion behaviour of CoCrMo alloys in 2 wt% sulphuric acid solution," *Electrochim. Acta*, vol. 125, pp. 543–555, Apr. 2014, doi: 10.1016/j.electacta.2014.01.143.

[18] Y. Yan, A. Neville, D. Dowson, and S. Williams, "Tribocorrosion in implants-assessing high carbon and low carbon Co-Cr-Mo alloys by in situ electrochemical measurements," *Tribol. Int.*, vol. 39, no. 12, pp. 1509–1517, 2006, doi: 10.1016/j.triboint.2006.01.016.

[19] Y. Yan, A. Neville, and D. Dowson, "Understanding the role of corrosion in the degradation of metal-on-metal implants," *Proc. Inst. Mech. Eng. Part H J. Eng. Med.*, vol. 220, no. 2, pp. 173–180, Jan. 2006, doi: 10.1243/095441105X63246.

[20] C. Xu, Z. Horita, and T. G. Langdon, “The evolution of homogeneity in an aluminum alloy processed using high-pressure torsion,” *Acta Mater.*, vol. 56, no. 18, pp. 5168–5176, Oct. 2008, doi: 10.1016/J.ACTAMAT.2008.06.036.

[21] P. Serre, R. B. Figueiredo, N. Gao, and T. G. Langdon, “Influence of strain rate on the characteristics of a magnesium alloy processed by high-pressure torsion,” *Mater. Sci. Eng. A*, vol. 528, no. 10–11, pp. 3601–3608, Apr. 2011, doi: 10.1016/J.MSEA.2011.01.066.

[22] R. B. Figueiredo, P. R. Cetlin, and T. G. Langdon, “Using finite element modeling to examine the flow processes in quasi-constrained high-pressure torsion,” *Mater. Sci. Eng. A*, vol. 528, no. 28, pp. 8198–8204, Oct. 2011, doi: 10.1016/J.MSEA.2011.07.040.

[23] M. Sage and C. Guillaud, “Méthode d’analyse quantitative des variétés allotropiques du cobalt par les rayons X,” *Rev. Métallurgie*, vol. 47, no. 2, pp. 139–145, Feb. 1950, doi: 10.1051/metal/195047020139.

[24] L. Ma, “Wear Behaviour of Biolox delta ceramic Composite for Joint Replacements,” no. January. The University of Sheffield, 2010, Accessed: Apr. 23, 2015. [Online]. Available: http://ethos.bl.uk/OrderDetails.do?uin=uk.bl.ethos.522486.

[25] C. Lentner, “Geigy Scientific Tables,” *Geigy Sci. tables*, pp. 1–41, 2014, Accessed: Aug. 11, 2018. [Online]. Available: https://ci.nii.ac.jp/naid/10019638328/.

[26] Y. C. Wang and T. G. Langdon, “Influence of phase volume fractions on the processing of a Ti–6Al–4V alloy by high-pressure torsion,” *Mater. Sci. Eng. A*, vol. 559, pp. 861–867, Jan. 2013, doi: 10.1016/J.MSEA.2012.09.034.

[27] H. Shahmir, F. Naghdi, P. H. R. Pereira, Y. Huang, and T. G. Langdon, “Factors

influencing superplasticity in the Ti-6Al-4V alloy processed by high-pressure torsion," *Mater. Sci. Eng. A*, vol. 718, pp. 198–206, Mar. 2018, doi: 10.1016/J.MSEA.2018.01.091.

[28] R. Namus, J. Nutter, J. Qi, and W. M. Rainforth, "The influence of protein concentration, temperature and cathodic polarization on the surface status of CoCrMo biomedical grade alloys," *Appl. Surf. Sci.*, vol. 499, p. 143908, Jan. 2020, doi: 10.1016/j.apsusc.2019.143908.

[29] R. Namus and W. M. Rainforth, "Influence of protein adsorption on tribocorrosion behaviour of CoCrMo biomedical-grade alloys," *Tribol. Int.*, p. 106364, Apr. 2020, doi: 10.1016/J.TRIBOINT.2020.106364.

[30] I. I. M. I. Hutchings and P. Shipway, *Tribology : friction and wear of engineering materials*. Butterworth-Heinemann, An imprint of Elsevier, 1992.

[31] A. Igual Muoz, N. Espallargas, A. Igual Muñoz, N. Espallargas, A. Igual Muoz, and N. Espallargas, "Tribocorrosion mechanisms in sliding contacts," in *Tribocorrosion of Passive Metals and Coatings*, Elsevier, 2011, pp. 118–152.

[32] J. R. Davis, *Corrosion : understanding the basics*. ASM International, 2000.

[33] A. C. C. Vieira, L. A. A. Rocha, N. Papageorgiou, and S. Mischler, "Mechanical and electrochemical deterioration mechanisms in the tribocorrosion of Al alloys in NaCl and in NaNO3 solutions," *Corros. Sci.*, vol. 54, no. 1, pp. 26–35, Jan. 2012, doi: 10.1016/j.corsci.2011.08.041.

[34] N. Papageorgiou and S. Mischler, "Electrochemical simulation of the current and potential response in sliding tribocorrosion," *Tribol. Lett.*, vol. 48, no. 3, pp. 271–283, 2012, doi: 10.1007/s11249-012-0022-9.

[35] S. Mischler, “Sliding tribo-corrosion of passive metals: mechanisms and modeling,” *Tribo-Corrosion Res. Testing, Appl., STP*, 2013, Accessed: Apr. 19, 2015. [Online]. Available: https://scholar.google.co.uk/scholar?q=Sliding+Tribo-Corrosion+of+Passive+Metals%3A+Mechanisms+and+Modeling&btnG=&hl=en&as_sdt=0%2C5&authuser=1#0.

[36] A. C. Fischer-Cripps, *Introduction to Contact Mechanics*. Boston, MA: Springer US, 2007.

[37] E. Martínez, J. Romero, A. Lousa, and J. Esteve, “Nanoindentation stress–strain curves as a method for thin-film complete mechanical characterization: application to nanometric CrN/Cr multilayer coatings,” *Appl. Phys. A*, vol. 77, no. 3–4, pp. 419–426, Aug. 2003, doi: 10.1007/s00339-002-1669-0.

[38] K. D. Ralston, N. Birbilis, and C. H. J. Davies, “Revealing the relationship between grain size and corrosion rate of metals,” *Scr. Mater.*, vol. 63, no. 12, pp. 1201–1204, 2010, doi: 10.1016/j.scriptamat.2010.08.035.

[39] T. Li, L. Liu, B. Zhang, Y. Li, F. Yan, N. Tao, F. Wang, “Passive behavior of a bulk nanostructured 316L austenitic stainless steel consisting of nanometer-sized grains with embedded nano-twin bundles,” *Corros. Sci.*, vol. 85, pp. 331–342, 2014, doi: 10.1016/j.corsci.2014.04.039.

[40] P. Peyre, X. Scherpereel, L. Berthe, C. Carboni, R. Fabbro, G. Béranger, C. Lemaitre, “Surface modifications induced in 316L steel by laser peening and shot-peening. Influence on pitting corrosion resistance,” vol. 280, no. 2, pp. 294–302, 2000, doi: 10.1016/S0921-5093(99)00698-X.

[41] A. Balyanov J. Kutnyakova, N.A. Amirkhanova, V.V. Stolyarov, R.Z. Valiev, X. Z. Liao, Y.H. Zhao, Y.B. Jiang, H.F. Xu, T.C. Lowe, Y.T. Zhu, “Corrosion resistance of

ultra fine-grained Ti," *Scr. Mater.*, vol. 51, no. 3, pp. 225–229, 2004, doi: 10.1016/j.scriptamat.2004.04.011.

[42] G. Purcek, O. Saray, O. Kul, I. Karaman, G.G. Yapici, M. Haouaoui, H.H. Maier, "Mechanical and wear properties of ultrafine-grained pure Ti produced by multi-pass equal-channel angular extrusion," *Mater. Sci. Eng. A*, vol. 517, no. 1–2, pp. 97–104, 2009, doi: 10.1016/j.msea.2009.03.054.

[43] C. T. Wang, N. Gao, R. J. K. K. Wood, and T. G. Langdon, "Wear Behaviour of Al-1050 Alloy Processed by Severe Plastic Deformation," *Mater. Sci. Forum*, vol. 667–669, pp. 1101–1106, Dec. 2010, doi: 10.4028/www.scientific.net/MSF.667-669.1101.

[44] T. Kucukomeroglu, "Effect of equal-channel angular extrusion on mechanical and wear properties of eutectic Al-12Si alloy," *Mater. Des.*, vol. 31, no. 2, pp. 782–789, 2010, doi: 10.1016/j.matdes.2009.08.004.

[45] A. I. Muñoz and S. Mischler, "Electrochemical Quartz Crystal Microbalance and X-Ray Photoelectron Spectroscopy study of cathodic reactions in Bovine Serum Albumin containing solutions on a Physical Vapour Deposition-CoCrMo biomedical alloy," *Electrochim. Acta*, vol. 180, pp. 96–103, Oct. 2015, doi: 10.1016/j.electacta.2015.08.017.

[46] R. Namus and W. M. Rainforth, "CoCrMo alloys in hip and knee replacements applications," University of Sheffield, 2018.

[47] A. J. Saldívar-García and H. F. López, "Microstructural effects on the wear resistance of wrought and as-cast Co-Cr-Mo-C implant alloys," *J. Biomed. Mater. Res. - Part A*, vol. 74, no. 2, pp. 269–74, Aug. 2005, doi: 10.1002/jbm.a.30392.

[48] A. R. Pelton, X. Gong, and T. Duerig, "Medical device materials: proceedings from

the Materials & Processes for Medical Devices Conference 2003," in *Smst-2003*, ASM International, 2004, pp. 199–204.